

# Isolated Attosecond $\gamma$ -Ray Pulse Generation with Transverse Orbital Angular Momentum Using Intense Spatiotemporal Optical Vortex Lasers

Fengyu Sun,<sup>1,2,3,\*</sup> Xinyu Xie,<sup>1,3,\*</sup> Wenpeng Wang,<sup>1,†</sup> Stefan Weber,<sup>4</sup> Xin Zhang,<sup>1</sup> Yuxin Leng,<sup>1</sup> Ruxin Li,<sup>1,2,‡</sup> and Zhizhan Xu<sup>1</sup>

<sup>1</sup>*State Key Laboratory of High Field Laser Physics and CAS Center for Excellence in Ultra-intense Laser Science, Shanghai Institute of Optics and Fine Mechanics (SIOM), Chinese Academy of Sciences (CAS), Shanghai 201800, China*

<sup>2</sup>*School of Physical Science and Technology, ShanghaiTech University, Shanghai 201210, China*

<sup>3</sup>*University of Chinese Academy of Sciences, Beijing 100049, China*

<sup>4</sup>*ELI Beamlines facility, Extreme Light Infrastructure ERIC, 25241 Dolni Brezany, Czech Republic*

(Dated: November 11, 2024)

An isolated attosecond vortex  $\gamma$ -ray pulse is generated by using a relativistic spatiotemporal optical vortex (STOV) laser in particle-in-cell simulations. A  $\sim 300$ -attosecond electron slice with transverse orbital angular momentum (TOAM) is initially selected and accelerated by the central spatiotemporal singularity of the STOV laser. This slice then collides with the laser's reflected Gaussian-like front from a planar target, initiating nonlinear Compton scattering and resulting in an isolated, attosecond ( $\sim 300$  as), highly collimated ( $\sim 4^\circ$ ), ultra-brilliant ( $\sim 5 \times 10^{24}$  photons/s/mm<sup>2</sup>/mrad<sup>2</sup>/0.1%BW at 1 MeV)  $\gamma$ -ray pulse. This STOV-driven approach overcomes the significant beam divergence and complex two-laser requirements of prior Gaussian-based methods while introducing TOAM to the attosecond  $\gamma$ -ray pulse, which opens avenues for ultrafast imaging, nuclear excitation, and detection applications.

The 2023 Noble Prize was awarded to Agostini, Krausz and L'Huillier for their pioneering work on generation of attosecond pulses [1–3]. Attosecond pulses were initially generated through high harmonic generation (HHG) using nonrelativistic laser-driven gas targets [4–6]. However, this approach typically results in a pulse train due to the multi-cycle nature of the driving laser [7, 8], rather than an isolated pulse, which is crucial for probing attosecond phenomena in electron physics by enabling undisturbed, single-shot observations [9, 10]. To address this, several methods have been proposed for generating isolated attosecond pulses, including the use of few-cycle laser pulses [8], polarization gating [11, 12], and other gating techniques [12, 13]. Despite these advances, the generated attosecond pulses were initially limited to the mid-infrared range, only extending into the soft X-ray region [14].

For higher-energy pulses,  $\gamma$ -ray pulses with  $\sim$ MeV-level photons have garnered increasing interest due to their potential applications in nuclear physics [9, 15], as typical reaction energies within the nucleus occur at the MeV scale [16]. Traditionally,  $\gamma$ -rays have been efficiently generated via nonlinear Thomson/Compton scattering [17–20] and nonlinear synchrotron radiation [21, 22] driven by relativistic lasers. To produce attosecond  $\gamma$ -rays, an approach using Gaussian lasers was initially proposed, where an isolated attosecond electron slice (IAES) is directly accelerated from an ultra-thin target and subsequently collides with an additional relativistic laser to generate an isolated attosecond  $\gamma$ -ray pulse [23]. However, this scheme faces two major challenges: the first is the significant divergence and low brightness of the  $\gamma$ -ray pulse, caused by the transverse ponderomotive force inherent to Gaussian laser fields [24, 25]; the second is the reliance on a two-laser

system, which requires precise spatiotemporal synchronization between the lasers [26, 27]. To address the first issue, structured laser pulses, such as Laguerre-Gaussian (LG) lasers, have been proposed. These lasers, with their hollow intensity distribution, can generate attosecond  $\gamma$ -ray trains with reduced divergence and enhanced brightness [28–31]. Unfortunately, these pulses are not isolated. A natural progression is to add attosecond temporal confinement to the spatial-vortex LG lasers, which could potentially resolve this limitation.

Fortunately, the spatiotemporal optical vortex (STOV) pulse possesses the desired characteristics, extending the vortex structure from the spatial domain into the spatiotemporal realm [32–35]. This pulse offers three promising advantages for attosecond  $\gamma$ -ray generation. First, the extremely small spatiotemporal singularity at the center of the STOV laser acts as an "attosecond selector" [36], enabling ultra-short, collimated particle modulation. Second, the front of the STOV laser exhibits a near-Gaussian intensity profile, which can be reflected and made to collide with particles at the singularity within a single-laser system, potentially simplifying experimental setups. Third, unlike traditional Gaussian or LG lasers, the STOV pulse imparts a novel transverse orbital angular momentum (TOAM) to the attosecond  $\gamma$ -ray, offering new dimensions for detection and triggering tools in various applications.

In this letter, we propose using an intense circularly polarized (CP) STOV laser to generate a collimated, ultrabright, and isolated attosecond  $\gamma$ -ray pulse with TOAM in three-dimensional (3D) particle-in-cell (PIC) simulations. Electrons are extracted and accelerated by the STOV laser's fields, forming an IAES. This slice collides with the reflected Gaussian-like laser front from a planar target to trigger the nonlinear Compton scattering (NCS) process, producing a highly collimated ( $\sim 4^\circ$ ) ultra-brilliant ( $\sim 5 \times 10^{24}$  photons/s/mm<sup>2</sup>/mrad<sup>2</sup>/0.1%BW at 1 MeV), and attosecond ( $\sim 300$  as)  $\gamma$ -ray pulse using  $\sim 10^{22}$  W/cm<sup>2</sup> laser intensity. Notably, TOAM is successfully transferred from the STOV laser to the  $\gamma$ -ray pulse, providing new opportunities for ultrahigh time resolution observation [37], nu-

\* These authors have contributed equally to this work.

† wangwenpeng@siom.ac.cn

‡ ruxinli@siom.ac.cn

clear selective excitation [38], and detection in nuclear science [9, 39].

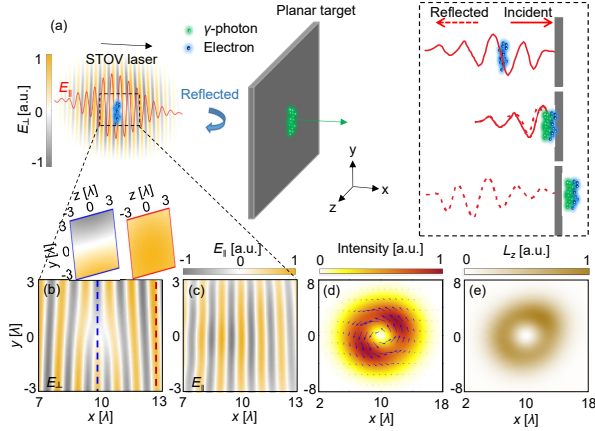


FIG 1. (a) Schematic of an isolated attosecond  $\gamma$ -ray pulse generation. An IAES collides with the self-reflected STOV laser, triggering the NCS process to generate the attosecond  $\gamma$ -ray pulse. (b) Vertical electric field and (c) longitudinal electric field distributions of the STOV laser. (d) The energy density of the STOV laser, with blue arrows indicating the circulating momentum flux. (e) TOAM density with the propagation term subtracted.

The generation of attosecond  $\gamma$ -ray pulse driven by the STOV laser was simulated using the 3D PIC code EPOCH [40, 41] [see Fig. 1 (a)]. An intense STOV laser, with a duration of  $\sim 30$  fs, propagates along the  $+x$  axis from the left side of the simulation box. The vertical electric field of the STOV laser pulse can be expressed as [see Fig. 1 (b)]:

$$\mathbf{E}_{\perp} = E_0 \frac{w_0}{w} \left( \frac{\xi^2 + y^2}{w^2} \right)^{\frac{l-1}{2}} \exp\left(-\frac{\xi^2 + y^2 + z^2}{w^2}\right) \times \exp[i(-l\phi_{st} + kx - \omega t + \phi_0)] \exp(i\hat{\mathbf{e}}_y + i\pi\sigma_z/2 \cdot \hat{\mathbf{e}}_z), \quad (1)$$

where  $E_0 = a_0 m_e c \omega / e$  is the peak amplitude of the electric field,  $a_0 = 70$  is the normalized laser amplitude (corresponding to the laser intensity  $I_0 = 1.35 \times 10^{22}$  W/cm $^2$ , which can be achieved under the current laboratory conditions [42–44]). The longitudinal coordinate local to the laser is  $\xi = ct - x$ , where  $c$  is the speed of light in vacuum.  $\omega = 4\lambda$  is the beam waist,  $\lambda = 1 \mu\text{m}$  is the laser center wavelength.  $l = 1$  is the topological charge number,  $\phi_{st} = \tan^{-1}(y/\xi)$  is the spatiotemporal azimuthal angle,  $k = 2\pi/\lambda$  is the wave number,  $\phi_0 = 0$  is the initial phase and  $\sigma_z = -1$  is the spin quantum number. Spatial and temporal profiles are used with  $\sqrt{\xi^2 + y^2}$ . The longitudinal electric field  $E_{\parallel}$  can be calculated using the Poisson equation:  $\mathbf{E}_{\parallel} = -(i/k)(\partial\mathbf{E}_{\perp}/\partial y + \partial\mathbf{E}_{\perp}/\partial z)$  [see Fig. 1 (c)].

$$\mathbf{E}_{\parallel} = E_0 \frac{i w_0}{k w} \exp\left[-\frac{\xi^2 + x^2 + y^2}{w^2} + i(-l\phi_{st} + kx - \omega t + \phi_0)\right] \times \exp(i\hat{\mathbf{e}}_x) \left[ \left( \frac{\xi^2 + y^2}{w^2} \right)^{\frac{1}{2}} \left( \frac{2z + 2y}{w^2} + \frac{ix}{x^2 + y^2} \right) - \frac{1}{2} \left( \frac{\xi^2 + y^2}{w^2} \right)^{-\frac{1}{2}} \frac{2y}{w^2} \right]. \quad (2)$$

Figure 1 (d) shows the time-averaged energy density of the STOV laser, which can be expressed as  $I = (\epsilon_0 |\mathbf{E}|^2 + |\mathbf{B}|^2 / \mu_0) / 4$  [45–47], where  $\mathbf{E}$  and  $\mathbf{B}$  represent the electric and magnetic fields of the STOV laser, while  $\epsilon_0$  and  $\mu_0$  are the dielectric constant and permeability of vacuum, respectively. Additionally, by subtracting the propagating momentum  $I/c$  in the  $+x$  direction, the energy flux circulates counterclockwise around the energy singularity, which can be calculated by the momentum vector  $\mathbf{P}_c = (P_x - I/c, P_y, P_z)$ , where the canonical momentum density  $\mathbf{P} = \text{Im}[\epsilon_0 \mathbf{E}^* \cdot (\nabla) \mathbf{E} + \mathbf{B}^* \cdot (\nabla) \mathbf{B} / \mu_0] / (4\omega)$  [48–50]. With the circulation of canonical momentum, the TOAM can be calculated as  $\mathbf{L} = \mathbf{r} \times \mathbf{P}_c$ , where  $\mathbf{r}$  is the local position relative to the energy centroid. By integrating the angular momentum density over the full space, the TOAM per photon for the STOV pulse is  $\sim 0.99\hbar$  [see Fig. 1 (e)]

The wire target is positioned between  $0 \mu\text{m}$  and  $4 \mu\text{m}$  with a diameter of  $400 \text{ nm}$ , and the planar target is positioned between  $40 \mu\text{m}$  and  $41 \mu\text{m}$  with a transverse area of  $16 \times 16 \mu\text{m}^2$ . Their initial density is  $100 n_c$ , composed of fully ionized hydrogen ions and electrons, where  $n_c = m_e \omega^2 / 4\pi e^2$  is the critical density,  $m_e$  is the electron mass,  $\omega$  is the laser frequency and  $e$  is the electron charge. The dimensions of the window are  $15 \mu\text{m} (x) \times 16 \mu\text{m} (y) \times 16 \mu\text{m} (z)$  with  $600 \times 640 \times 640$  cells. Each cell contains 50 macro-particles for the wire target and 8 macro-particles for the planar target. Absorption boundary conditions are employed for both particles and fields.

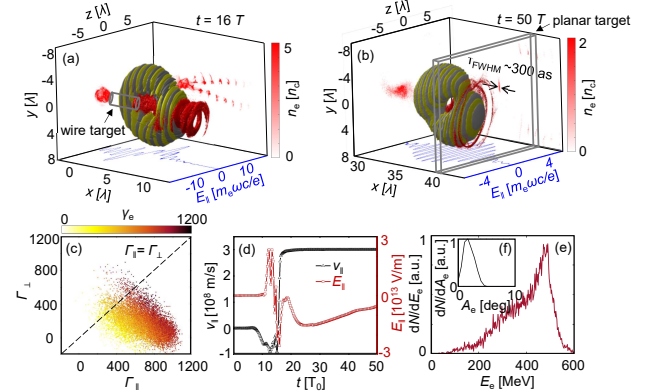


FIG 2. Energy density iso-surface at (a)  $t = 16T_0$  ( $T_0 = \lambda/c$ ) with  $500 \text{ MeV} \cdot n_c$  and (b)  $t = 50T_0$  with  $1 \text{ GeV} \cdot n_c$ ; as well as the one-dimensional longitudinal electric field in the  $x-y$  plane. (c) Energy-gain plane of  $\Gamma_{\parallel}$  and  $\Gamma_{\perp}$  of electrons, with their net  $\gamma_e$ -factor color-coded. (d) Average longitudinal electron speed  $v_{\parallel}$  and experienced average longitudinal electric field  $E_{\parallel}$  of the IAES as a function of  $T_0$ . (e) Energy spectrum and (f) divergence angle of the IAES.

When an intense STOV laser irradiates a wire target, electrons are expelled from the optical axis due to the transverse ponderomotive force  $F_p = -m_e c^2 / (4\gamma_e) \nabla E^2(x, y)$ . This occurs because the front of the vertical electric field of the STOV laser resembles that of a Gaussian mode laser [see Fig. 1 (b) and Fig. 2 (a)], where  $E$  is the normalized laser amplitude derived from Eq. 1,  $\gamma_e = (1 - v^2/c^2)^{-1/2}$  is the relativistic parameter,  $v$  is the electron speed. Consequently, only those electrons located at

the laser phase singularity can be trapped within the laser field [see Fig. 2 (b)]. Additionally, the longitudinal electric field ( $E_{\parallel}$ ) establishes an accelerating configuration within the hollow structure, enabling the acceleration of trapped electrons.

To investigate the acceleration mechanism in detail, Fig. 2 (c) presents the energy gain plane ( $\Gamma_{\parallel}, \Gamma_{\perp}$ ) for the IAES, where  $\Gamma_{\parallel} = -\int_0^t ev_{\parallel} E_{\parallel} dt$  and  $\Gamma_{\perp} = -\int_0^t ev_{\perp} E_{\perp} dt$  denote the accumulated energy gains from the longitudinal and transverse fields, respectively [51]. It is observed that the most energetic electrons are primarily accelerated by the longitudinal field, with the number of electrons accelerated longitudinally significantly exceeding that of those accelerated transversely. Therefore, the IAES is predominantly accelerated by the longitudinal electric field  $E_{\parallel}$ . It is noted that a brief yet intense longitudinal electric field of  $E_{\parallel} \sim 10^{13}$  V/m boosts the electron energy of  $\gamma_e \sim 30$ , primarily driven by the strong longitudinal component  $E_{\parallel}$  of the diffracted laser field at  $16 T_0$  [see Fig. 2 (d)]. After  $t = 16T_0$ , such electrons traveling at speeds close to the light speed continue to accelerate to form the IAES within the same phase since the longitudinal field remains negative.

Finally, this phase-locked acceleration enables the IAES within the spatiotemporal phase singularity of the STOV laser to achieve a cut-off energy of  $\sim 600$  MeV [see Fig. 2 (e)], a charge of around 0.2 nC, and a divergence of about  $2^{\circ}$  [see Fig. 2 (f)] with a full width at half maximum (FWHM) of  $\sim 300$  as. Unlike traditional Gaussian lasers, which cause the wire target to expel electrons due to the transverse pondermotive force, this force induces a divergence of the electrons without exhibiting localized properties.

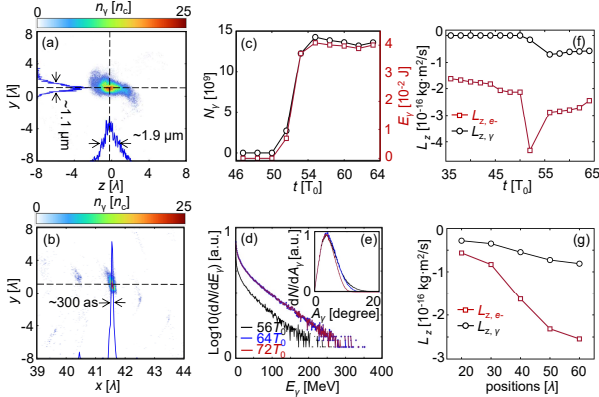


FIG 3. Density distribution of the isolated attosecond  $\gamma$ -ray pulse in the (a)  $z - y$  plane and (b)  $x - y$  plane at  $t = 56T_0$ , with the blue line indicating the one-dimensional distribution along the line of black dashes. (c) Evolution of the photon number and the photon energy of the  $\gamma$ -ray pulse. (d) Energy spectra and (e) angular divergence of the  $\gamma$ -ray pulse at  $t = 56 T_0$ ,  $64 T_0$ , and  $72 T_0$ . (f) Evolution of TOAM for the IAES and  $\gamma$ -ray pulse with the plane target at  $x = 40 \mu\text{m}$ . (g) TOAM of the IAES and the  $\gamma$ -ray pulse at different plane target positions.

The hundreds-of-MeV IAES depicted in Fig. 2 demonstrate its efficacy as a particle source for subsequent attosecond  $\gamma$ -ray generation. In this process, a planar target reflects the

Gaussian-like front of the STOV laser, resulting in a collision with the IAES within the singularity of the STOV laser. This interaction triggers the NCS process, leading to the generation of an isolated attosecond  $\gamma$ -ray pulse [see Figs. 3 (a) and (b)] [18, 20].

To facilitate the efficient emission of attosecond  $\gamma$ -rays, the quantum electrodynamics (QED) effects in photon radiation are characterized by the nonlinear QED parameter  $\chi_e \equiv |e|\hbar/(m_e^3 c^4) \sqrt{-(F_{\mu\nu} p^\nu)}$  [52], where  $\chi_e \geq 0.1$  [53]. Here,  $\hbar$  is the reduced Planck constant,  $F_{\mu\nu}$  is the field tensor, and  $p^\nu$  is the electron four-momentum. In our scheme,  $\chi_e$  can be expressed by  $\chi_e = \gamma_e |\mathbf{E}_{\perp} + \boldsymbol{\beta} \times c\mathbf{B}|/E_S$ , where  $\boldsymbol{\beta} = \mathbf{v}/c$  is the normalization electron velocity,  $\mathbf{B}$  is the magnetic field, and  $E_S = 1.3 \times 10^{18}$  V/m is the Schwinger field [54].

When the laser propagates in the same direction as the IAES (along the  $+x$  direction),  $\mathbf{E}_{\perp}$  can be almost completely canceled by  $\boldsymbol{\beta} \times c\mathbf{B}$ , resulting in  $\chi_e \approx 0$ . This condition inhibits the emission of high-energy  $\gamma$  photons before  $t = 50T_0$ . By contrast, after  $t = 50T_0$ , the quantum parameter  $\chi_e$  reaches 0.3 due to the collision between the reflected STOV laser (propagating in the  $-x$  direction) and the high-energy IAES (propagating in the  $+x$  direction), indicating a significant enhancement in attosecond  $\gamma$ -ray emission.

The power of the attosecond  $\gamma$ -ray emitted by the electron can be expressed as  $P_{\text{rad}} \approx 2eE_S N_e c \alpha_f \chi_e^2 g(\chi_e)/3$ , where  $N_e$  is the number of IAES,  $\alpha_f$  is the fine-structure constant, and  $g(\chi_e) \approx (3.7\chi_e^3 + 31\chi_e^2 + 12\chi_e + 1)^{-4/9}$  is the radiation correction induced by the QED effects [55]. Starting from  $t = 50T_0$ , as the instantaneous radiation power  $P_{\text{rad}}$  increases, both the photon number and energy of the attosecond  $\gamma$ -ray experience significant growth [see Fig. 3 (c)]. By  $t = 56T_0$ , the generation of  $\gamma$  photons is essentially complete, marking the end of the NCS process. At this point, the photon energy and divergence angle of the attosecond  $\gamma$ -ray reach  $\sim 300$  MeV and  $\sim 70$  mrad, respectively [see Figs. 3 (d) and (e)].

According to the pulse width of the IAES  $\tau_e$  and the reflected STOV laser  $\tau_L$ , the generated pulse width of  $\gamma$ -ray can be described as  $\tau_\gamma = \tau_e + \tau_L/(4\gamma_e^2) \approx 300$  as [56, 57], which is similar to the PIC simulation results [see Fig. 3 (b)]. Such an isolated  $\gamma$ -ray pulse, with the photon number exceeding  $\sim 10^{10}$  at 1 MeV, has a transverse dimension of about  $1.1 \times 1.9 \mu\text{m}^2$ . This configuration results in an isolated collimated  $\gamma$ -ray source with the peak brilliance of  $\sim 5 \times 10^{24}$  photons/s/mm<sup>2</sup>/mrad<sup>2</sup>/0.1%BW, significantly exceeding the brilliance achieved in current attosecond  $\gamma$ -ray studies [18, 58, 59].

Since the STOV laser pulse carries an intrinsic TOAM  $\sim 0.99\hbar$  value [see Fig. 1 (e)], there is the possibility for TOAM transfer during the generation of the isolated attosecond  $\gamma$ -ray pulse. The TOAM is an extrinsic property of particle pulses; thus, the TOAM of the IAES and the  $\gamma$ -ray pulse can be calculated in the laboratory frame using  $L_z = \sum_i (xp_{iy} - yp_{ix})$ , where  $i$  represents the index of the particles in the IAES and  $\gamma$ -ray pulse. The generated photons propagate in the direction of the electron motion, and their momentum originates from the parent electrons [53]. This interaction results in the generated isolated attosecond  $\gamma$ -ray carrying a TOAM of  $\sim 0.5 \times 10^{-16}$  kg-m<sup>2</sup>/s, with the TOAM of the  $\gamma$ -ray pulse grad-

ually stabilizing at the end of the interaction [see Fig. 3 (f)]. Such an isolated attosecond  $\gamma$ -ray pulse with TOAM presents new opportunities in nuclear physics and has garnered significant attention for its potential applications, such as modulating photonuclear reaction rates [60], uncovering novel spin phenomena [61, 62], disentangling spin states and dual resonances [63], and introducing innovative multipolar analyses in photonuclear reactions [64].

From the above analysis, it is clear that the TOAM of the attosecond  $\gamma$ -ray pulse originates from the TOAM of the colliding IAES, which, in turn, is imparted by the STOV laser. To further confirm this phenomenon, a planar target can be placed at a distance of  $20\ \mu\text{m}$  to  $60\ \mu\text{m}$  to reflect the STOV laser, thus influencing the interaction time between the STOV laser and the IAES [see Fig. 3 (g)]. During the electron acceleration process, the TOAM of the electrons increases as the distance between the wire target and the planar target grows. This increase results from the continuous transfer of TOAM from the STOV laser to the IAES. Moreover, in the NCS process, the electrons transfer their TOAM to the  $\gamma$  photons, leading to a corresponding increase in the TOAM of the  $\gamma$  photons as the electron TOAM rises.

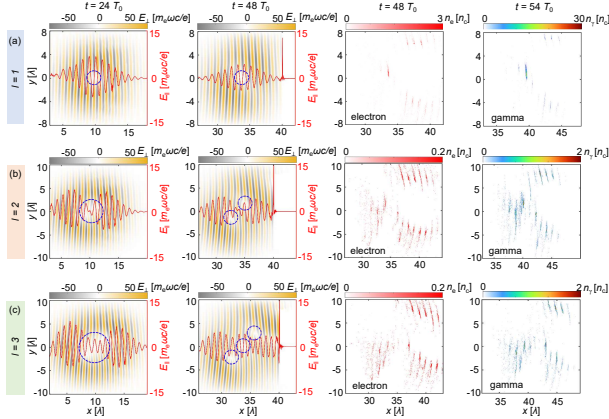


FIG 4. Vertical electric field  $E_{\perp}$  and one-dimensional longitudinal electric field  $E_{\parallel}$  on axis at  $t = 24T_0$  and  $t = 48T_0$ ; electron distribution in the  $x - y$  plane at  $t = 48T_0$ ;  $\gamma$ -photon distribution in the  $x - y$  plane at  $t = 54T_0$  driven by the (a)  $l = 1$ , (b) 2 and (c) 3 of the STOV laser. The blue dashed circle indicates the positions of the phase singularity.

It is important to note that the spatiotemporal phase singular-

ity structure is also present at the laser center for STOV lasers with higher-order topological charges ( $l = 2$  and  $l = 3$ ) [see Figs. 4 (b) and (c)]. Unlike the case of  $l = 1$  [see Fig. 4 (a)], the phase difference between the upper and lower laser stripes is  $4\pi$  and  $6\pi$  for  $l = 2$  and  $l = 3$ , respectively, generating  $l$  electron slices within the phase singularity. Moreover, due to the spatial diffraction and structural instability, the higher-order STOV laser field evolves from one single singularity to  $l$  singularities during laser propagation [65]. This reduces the convergence effect of the vertical electric field on the electron slices, leading to increased transverse electron divergence. These electron slices produce multiple diverging attosecond  $\gamma$ -ray pulses through the NCS process. It is also noteworthy that for higher-order STOV fields ( $l = 2$  and  $l = 3$ ), the longitudinal electric field  $E_{\parallel}$  within the phase singularity is weaker compared to the  $l = 1$  case, which limits electron acceleration. Therefore, in our study, the STOV field with  $l = 1$  proves to be a more suitable structure for generating isolated attosecond  $\gamma$ -ray pulse.

In conclusion, this study proposed an all-optical scheme for generating isolated attosecond  $\gamma$ -ray pulse with TOAM using an intense CP STOV laser on a wire target, as demonstrated through 3D PIC simulations. We found that an IAES, characterized by  $\sim 300$  as duration,  $\sim 0.2$  nC charge,  $\sim 2^\circ$  divergence angle, and  $\sim 600$  MeV cutoff energy, is initially modulated by the spatiotemporal singularity fields at the center of the STOV laser. This pulse subsequently collides with the reflected Gaussian-like front of the planar target, leading to the NCS process that produces an isolated attosecond  $\gamma$ -ray pulse with a duration of  $\sim 300$  as, a divergence angle of  $\sim 4^\circ$ , and an extraordinary brilliance of  $\sim 5 \times 10^{24}$  photons/s/mm<sup>2</sup>/mrad<sup>2</sup>/0.1%BW at 1 MeV  $\gamma$ -ray pulse. Unlike previous  $\gamma$ -ray sources driven by traditional Gaussian lasers, this novel  $\gamma$ -ray pulse carries a distinct TOAM, introducing revolutionary capabilities for relativistic modulation that could enable ultra-high time-resolution observations, selective nuclear excitation, and enhanced detection in nuclear science.

*Acknowledgments:* We thank Prof. B.-S. Xie, Dr. C.-W. Zhang and Dr. H. Zhang for fruitful discussions. This study is supported by the Natural Science Foundation of China (Grant No. 12075306), Natural Science Foundation of Shanghai (Grant No. 22ZR1470900), Key Research Programs in Frontier Science (Grant No. ZDBSLY-SLH006), Strategic Priority Research Program of the Chinese Academy of Sciences (Grant No. XDA0380000), Shanghai Science and Technology Committee Program (Grant No. 22DZ1100300).

[1] P. Agostini, Nobel lecture: Genesis and applications of attosecond pulse trains, *Rev. Mod. Phys.* **96**, 030501 (2024).  
 [2] F. Krausz, Nobel lecture: Sub-atomic motions, *Rev. Mod. Phys.* **96**, 030502 (2024).  
 [3] A. L’Huillier, Nobel lecture: The route to attosecond pulses, *Rev. Mod. Phys.* **96**, 030503 (2024).  
 [4] G. Sansone, L. Poletto, and M. Nisoli, High-energy attosecond light sources, *Nat. Photonics* **5**, 655–663 (2011).  
 [5] M. Yeung, S. Rykovanov, J. Bierbach, L. Li, E. Eckner,

S. Kuschel, A. Woldegeorgis, C. Rödel, A. Sävert, G. G. Paulus, M. Coughlan, B. Dromey, and M. Zepf, Experimental observation of attosecond control over relativistic electron bunches with two-colour fields, *Nat. Photonics* **11**, 32–35 (2017).  
 [6] U. Teubner and P. Gibbon, High-order harmonics from laser-irradiated plasma surfaces, *Rev. Mod. Phys.* **81**, 445 (2009).  
 [7] P. Antoine, A. L’Huillier, and M. Lewenstein, Attosecond pulse trains using high-order harmonics, *Phys. Rev. Lett.* **77**, 1234 (1996).

- [8] P. M. Paul, E. S. Toma, P. Breger, G. Mullot, F. Augé, P. Balcou, H. G. Muller, and P. Agostini, Observation of a train of attosecond pulses from high harmonic generation, *Science* **292**, 1689 (2001).
- [9] K. W. D. Ledingham, P. McKenna, and R. P. Singhal, Applications for nuclear phenomena generated by ultra-intense lasers, *Science* **300**, 1107 (2003).
- [10] Y. X. Zhang, S. Rykovanov, M. Shi, C. L. Zhong, X. T. He, B. Qiao, and M. Zepf, Giant isolated attosecond pulses from two-color laser-plasma interactions, *Phys. Rev. Lett.* **124**, 114802 (2020).
- [11] M. Yeung, B. Dromey, S. Cousens, T. Dzelzainis, D. Kiefer, J. Schreiber, J. H. Bin, W. Ma, C. Kreuzer, J. Meyer-ter Vehn, M. J. V. Streeter, P. S. Foster, S. Rykovanov, and M. Zepf, Dependence of laser-driven coherent synchrotron emission efficiency on pulse ellipticity and implications for polarization gating, *Phys. Rev. Lett.* **112**, 123902 (2014).
- [12] S. G. Rykovanov, M. Geissler, J. M. ter Vehn, and G. D. Tsakiris, Intense single attosecond pulses from surface harmonics using the polarization gating technique, *New J. Phys.* **10**, 025025 (2008).
- [13] P. Heissler, R. Hörlein, J. M. Mikhailova, L. Waldecker, P. Tzallas, A. Buck, K. Schmid, C. M. S. Sears, F. Krausz, L. Veisz, M. Zepf, and G. D. Tsakiris, Few-cycle driven relativistically oscillating plasma mirrors: A source of intense isolated attosecond pulses, *Phys. Rev. Lett.* **108**, 235003 (2012).
- [14] F. Krausz and M. Ivanov, Attosecond physics, *Rev. Mod. Phys.* **81**, 163 (2009).
- [15] J.-X. Li, K. Z. Hatsagortsyan, B. J. Galow, and C. H. Keitel, Attosecond gamma-ray pulses via nonlinear Compton scattering in the radiation-dominated regime, *Phys. Rev. Lett.* **115**, 204801 (2015).
- [16] V. G. Nedorezov, S. G. Rykovanov, and A. B. Savel'ev, Nuclear photonics: results and prospects, *Physics-Uspekhi* **64**, 1214 (2021).
- [17] Y.-J. Gu, O. Klimo, S. V. Bulanov, and S. Weber, Brilliant gamma-ray beam and electron-positron pair production by enhanced attosecond pulses, *Commun. Phys.* **1**, 93 (2018).
- [18] G. Sarri, D. J. Corvan, W. Schumaker, J. M. Cole, A. Di Piazza, H. Ahmed, C. Harvey, C. H. Keitel, K. Krushelnick, S. P. D. Mangles, Z. Najmudin, D. Symes, A. G. R. Thomas, M. Yeung, Z. Zhao, and M. Zepf, Ultrahigh brilliance multi-MeV  $\gamma$ -ray beams from nonlinear relativistic Thomson scattering, *Phys. Rev. Lett.* **113**, 224801 (2014).
- [19] S. Cipiccia, M. R. Islam, B. Ersfeld, R. P. Shanks, E. Brunetti, G. Vieux, X. Yang, R. C. Issac, S. M. Wiggins, G. H. Welsh, M.-P. Anania, D. Maneuski, R. Montgomery, G. Smith, M. Hoek, D. J. Hamilton, N. R. C. Lemos, D. Symes, P. P. Rajeev, V. O. Shea, J. M. Dias, and D. A. Jaroszynski, Gamma-rays from harmonically resonant betatron oscillations in a plasma wake, *Nat. Phys.* **7**, 867–871 (2011).
- [20] K. Ta Phuoc, S. Corde, C. Thauray, V. Malka, A. Tafzi, J. P. Goddet, R. C. Shah, S. Sebban, and A. Rousse, All-optical Compton gamma-ray source, *Nat. Photonics* **6**, 308–311 (2012).
- [21] W.-M. Wang, Z.-M. Sheng, P. Gibbon, L.-M. Chen, Y.-T. Li, and J. Zhang, Collimated ultrabright gamma rays from electron wiggling along a petawatt laser-irradiated wire in the QED regime, *Proc. Natl. Acad. Sci. U. S. A.* **115**, 9911 (2018).
- [22] X.-L. Zhu, M. Chen, S.-M. Weng, T.-P. Yu, W.-M. Wang, F. He, Z.-M. Sheng, P. McKenna, D. A. Jaroszynski, and J. Zhang, Extremely brilliant GeV  $\gamma$ -rays from a two-stage laser-plasma accelerator, *Sci. Adv.* **6**, eaaz7240 (2020).
- [23] L.-Q. Zhang, K. Liu, S. Tang, W. Luo, J. Zhao, H. Zhang, and T.-P. Yu, Generation of isolated and polarized  $\gamma$ -ray pulse by few-cycle laser irradiating a nanofoil, *Plasma Phys. Control. Fusion* **64**, 105011 (2022).
- [24] Y. Tian, J. Liu, W. Wang, C. Wang, A. Deng, C. Xia, W. Li, L. Cao, H. Lu, H. Zhang, Y. Xu, Y. Leng, R. Li, and Z. Xu, Electron emission at locked phases from the laser-driven surface plasma wave, *Phys. Rev. Lett.* **109**, 115002 (2012).
- [25] M. Thévenet, A. Leblanc, S. Kahaly, H. Vincenti, A. Vernier, F. Quéré, and J. Faure, Vacuum laser acceleration of relativistic electrons using plasma mirror injectors, *Nat. Phys.* **12**, 355–360 (2016).
- [26] H.-Z. Li, T.-P. Yu, L.-X. Hu, Y. Yin, D.-B. Zou, J.-X. Liu, W.-Q. Wang, S. Hu, and F.-Q. Shao, Ultra-bright  $\gamma$ -ray flashes and dense attosecond positron bunches from two counter-propagating laser pulses irradiating a micro-wire target, *Opt. Express* **25**, 21583 (2017).
- [27] J. Zhao, Y.-T. Hu, Y. Lu, H. Zhang, L.-X. Hu, X.-L. Zhu, Z.-M. Sheng, I. C. E. Turcu, A. Pukhov, F.-Q. Shao, and T.-P. Yu, All-optical quasi-monoenergetic GeV positron bunch generation by twisted laser fields, *Commun. Phys.* **5**, 15 (2022).
- [28] L. Allen, M. W. Beijersbergen, R. J. C. Spreeuw, and J. P. Woerdman, Orbital angular momentum of light and the transformation of Laguerre-Gaussian laser modes, *Phys. Rev. A* **45**, 8185 (1992).
- [29] W. P. Wang, C. Jiang, B. F. Shen, F. Yuan, Z. M. Gan, H. Zhang, S. H. Zhai, and Z. Z. Xu, New optical manipulation of relativistic vortex cutter, *Phys. Rev. Lett.* **122**, 024801 (2019).
- [30] W. Wang, B. Shen, X. Zhang, L. Zhang, Y. Shi, and Z. Xu, Hollow screw-like drill in plasma using an intense Laguerre-Gaussian laser, *Sci. Rep.* **5**, 8274 (2015).
- [31] L. Ju, C. Zhou, T. Huang, K. Jiang, C. Wu, T. Long, L. Li, H. Zhang, M. Yu, and S. Ruan, Generation of collimated bright gamma rays with controllable angular momentum using intense Laguerre-Gaussian laser pulses, *Phys. Rev. Appl.* **12**, 014054 (2019).
- [32] K. Y. Bliokh and F. Nori, Spatiotemporal vortex beams and angular momentum, *Phys. Rev. A* **86**, 033824 (2012).
- [33] N. Jhajj, I. Larkin, E. W. Rosenthal, S. Zahedpour, J. K. Wahlstrand, and H. M. Milchberg, Spatiotemporal optical vortices, *Phys. Rev. X* **6**, 031037 (2016).
- [34] A. Chong, C. Wan, J. Chen, and Q. Zhan, Generation of spatiotemporal optical vortices with controllable transverse orbital angular momentum, *Nat. Photonics* **14**, 350–354 (2020).
- [35] C. Wan, Q. Cao, J. Chen, A. Chong, and Q. Zhan, Toroidal vortices of light, *Nat. Photonics* **16**, 519–522 (2022).
- [36] F. Sun, W. Wang, H. Dong, J. He, Z. Shi, Z. Lv, Q. Zhan, Y. Leng, S. Zhuang, and R. Li, Generation of isolated attosecond electron sheet via relativistic spatiotemporal optical manipulation, *Phys. Rev. Res.* **6**, 013075 (2024).
- [37] M. Drescher, M. Hentschel, R. Kienberger, M. Uiberacker, V. Yakovlev, A. Scrinzi, T. Westerwalbesloh, U. Kleineberg, U. Heinzmann, and F. Krausz, Time-resolved atomic inner-shell spectroscopy, *Nature* **419**, 803–807 (2002).
- [38] Z.-W. Lu, L. Guo, Z.-Z. Li, M. Ababekri, F.-Q. Chen, C. Fu, C. Lv, R. Xu, X. Kong, Y.-F. Niu, and J.-X. Li, Manipulation of giant multipole resonances via vortex  $\gamma$  photons, *Phys. Rev. Lett.* **131**, 202502 (2023).
- [39] D. Habs, T. Tajima, J. Schreiber, C. P. Barty, M. Fujiwara, and P. G. Thirolf, Vision of nuclear physics with photo-nuclear reactions by laser-driven  $\gamma$  beams, *Eur. Phys. J. D* **55**, 279–285 (2009).
- [40] T. D. Arber, K. Bennett, C. S. Brady, A. Lawrence-Douglas, M. G. Ramsay, N. J. Sircombe, P. Gillies, R. G. Evans, H. Schmitz, A. R. Bell, and C. P. Ridgers, Contemporary particle-in-cell approach to laser-plasma modelling, *Plasma Phys. Control. Fusion* **57**, 113001 (2015).

- [41] C. Ridgers, J. Kirk, R. Ducloux, T. Blackburn, C. Brady, K. Bennett, T. Arber, and A. Bell, Modelling gamma-ray photon emission and pair production in high-intensity laser-matter interactions, *J. Comput. Phys.* **260**, 273 (2014).
- [42] W. Li, Z. Gan, L. Yu, C. Wang, Y. Liu, Z. Guo, L. Xu, M. Xu, Y. Hang, Y. Xu, J. Wang, P. Huang, H. Cao, B. Yao, X. Zhang, L. Chen, Y. Tang, S. Li, X. Liu, S. Li, M. He, D. Yin, X. Liang, Y. Leng, R. Li, and Z. Xu, 339 J high-energy Ti:sapphire chirped-pulse amplifier for 10 PW laser facility, *Opt. Lett.* **43**, 5681 (2018).
- [43] C. N. Danson, C. Haefner, J. Bromage, T. Butche, J.-C. F. Chanteloup, E. A. Chowdhury, A. Galvanauskas, L. A. Gizzi, J. Hein, D. I. Hillier, N. W. Hopps, Y. Kato, E. A. Khazanov, R. Kodama, G. Korn, R. Li, Y. Li, J. Limpert, J. Ma, C. H. Nam, D. Neely, D. Papadopoulos, R. R. Penman, L. Qian, J. J. Rocca, A. A. Shaykin, C. W. Siders, C. Spindloe, S. Szatmári, R. M. G. M. Trines, J. Zhu, P. Zhu, and J. D. Zuegel, Petawatt and exawatt class lasers worldwide, *High Power Laser Sci. Eng.* **7**, e54 (2019).
- [44] J. W. Yoon, Y. G. Kim, I. W. Choi, J. H. Sung, H. W. Lee, S. K. Lee, and C. H. Nam, Realization of laser intensity over  $10^{23}$  W/cm<sup>2</sup>, *Optica* **8**, 630 (2021).
- [45] L. Zhang, L. Ji, and B. Shen, Intense harmonic generation driven by a relativistic spatiotemporal vortex beam, *High Power Laser Sci. Eng.* **10**, e46 (2022).
- [46] C.-W. Zhang, D.-S. Zhang, and B.-S. Xie, Generation of gamma photons and pairs with transverse orbital angular momentum via spatiotemporal optical vortex pulse, *Phys. Plasmas* **31**, 073106 (2024).
- [47] L. B. Ju, C. N. Wu, M. Y. Yu, T. W. Huang, H. Zhang, S. Z. Wu, C. T. Zhou, and S. C. Ruan, Isolated attosecond electron and hard x-ray pulse generation by ultra-intense spatiotemporal vortex laser, *New J. Phys.* **26**, 053020 (2024).
- [48] K. Y. Bliokh, Y. S. Kivshar, and F. Nori, Magnetolectric effects in local light-matter interactions, *Phys. Rev. Lett.* **113**, 033601 (2014).
- [49] K. Y. Bliokh, A. Y. Bekshaev, and F. Nori, Extraordinary momentum and spin in evanescent waves, *Nat. Commun.* **5**, 3300 (2014).
- [50] K. Y. Bliokh, A. Y. Bekshaev, A. G. Kofman, and F. Nori, Photon trajectories, anomalous velocities and weak measurements: a classical interpretation, *New J. Phys.* **15**, 073022 (2013).
- [51] X. Shen, A. Pukhov, and B. Qiao, High-flux bright x-ray source from femtosecond laser-irradiated microtapes, *Commun. Phys.* **7**, 84 (2024).
- [52] V. I. Ritus, Quantum effects of the interaction of elementary particles with an intense electromagnetic field, *J. Sov. Laser Res.* **6**, 497 (1985).
- [53] X.-L. Zhu, M. Chen, T.-P. Yu, S.-M. Weng, L.-X. Hu, P. McKenna, and Z.-M. Sheng, Bright attosecond  $\gamma$ -ray pulses from nonlinear Compton scattering with laser-illuminated compound targets, *Appl. Phys. Lett.* **112**, 174102 (2018).
- [54] J. Schwinger, On gauge invariance and vacuum polarization, *Phys. Rev.* **82**, 664 (1951).
- [55] M. J. Duff, R. Capdessus, D. D. Sorbo, C. P. Ridgers, M. King, and P. McKenna, Modelling the effects of the radiation reaction force on the interaction of thin foils with ultra-intense laser fields, *Plasma Phys. Control. Fusion* **60**, 064006 (2018).
- [56] I. V. Pogorelsky, I. Ben-Zvi, T. Hirose, S. Kashiwagi, V. Yakimenko, K. Kusche, P. Siddons, J. Skaritka, T. Kumita, A. Tsunemi, T. Omori, J. Urakawa, M. Washio, K. Yokoya, T. Okugi, Y. Liu, P. He, and D. Cline, Demonstration of  $8 \times 10^{18}$  photons/second peaked at 1.8 Å in a relativistic thomson scattering experiment, *Phys. Rev. ST Accel. Beams* **3**, 090702 (2000).
- [57] W. Luo, H. B. Zhuo, Y. Y. Ma, Y. M. Song, Z. C. Zhu, T. P. Yu, and M. Y. Yu, Attosecond Thomson-scattering x-ray source driven by laser-based electron acceleration, *Appl. Phys. Lett.* **103**, 174103 (2013).
- [58] H. Zhang, J. Zhao, Y. Hu, Q. Li, Y. Lu, Y. Cao, D. Zou, Z. Sheng, F. Pegoraro, P. McKenna, F. Shao, and Y. Tongpu, Efficient bright  $\gamma$ -ray vortex emission from a laser-illuminated light-fan-in-channel target, *High Power Laser Sci. Eng.* **9**, e43 (2021).
- [59] Y.-T. Hu, J. Zhao, H. Zhang, Y. Lu, W.-Q. Wang, L.-X. Hu, F.-Q. Shao, and T.-P. Yu, Attosecond  $\gamma$ -ray vortex generation in near-critical-density plasma driven by twisted laser pulses, *Appl. Phys. Lett.* **118**, 054101 (2021).
- [60] A. Afanasev, V. G. Serbo, and M. Solyanik, Radiative capture of cold neutrons by protons and deuteron photodisintegration with twisted beams, *J. Phys. G Nucl. Part. Phys.* **45**, 055102 (2018).
- [61] A. Afanasev, C. E. Carlson, and M. Solyanik, Circular dichroism of twisted photons in non-chiral atomic matter, *J. Opt.* **19**, 105401 (2017).
- [62] I. P. Ivanov, N. Korchagin, A. Pimikov, and P. Zhang, Doing spin physics with unpolarized particles, *Phys. Rev. Lett.* **124**, 192001 (2020).
- [63] I. P. Ivanov, N. Korchagin, A. Pimikov, and P. Zhang, Kinematic surprises in twisted-particle collisions, *Phys. Rev. D* **101**, 016007 (2020).
- [64] A. Afanasev, C. E. Carlson, and M. Solyanik, Atomic spectroscopy with twisted photons: Separation of M1-E2 mixed multipoles, *Phys. Rev. A* **97**, 023422 (2018).
- [65] M. A. Porras, Propagation of higher-order spatiotemporal vortices, *Opt. Lett.* **48**, 367 (2023).